Sr 1/2 Ce 5/14 □ 1/7 WO 4: a new modulated ternary scheelite compound

Rafael Hernandez Damascena dos Passos, Madjid Arab, Carlson Pereira de Souza, Christine Leroux

▶ **To cite this version:**

HAL Id: hal-01541637
https://univ-tln.hal.science/hal-01541637

Sr$_{1/2}$Ce$_{5/14}\square_{1/7}$WO$_4$: a new modulated ternary scheelite compound

Rafael Hernandez Damascena dos Passos, Madjid Arab, Carlson Pereira de Souza and Christine Leroux

Sr$_{1/2}$Ce$_{5/14}$□$_{1/7}$WO$_4$: a new modulated ternary scheelite compound

Rafael Hernandez Damascena dos Passos,[a,b] Madjid Arab,[a] Carlson Pereira de Souza[b] and Christine Leroux[a]*

[a]Université de Toulon, CNRS, IM2NP, BP 20132, La Garde CEDEX, F- 83957, France, and [b]Universidade do Rio Grande de Norte, DEQ/PPGEQ-LMNRC, Campus Universitario, Lagoa Nova 59072-970 Natal, Brazil. *Correspondence e-mail: leroux@univ-tln.fr

For the first time, a ternary tetragonal scheelite structure tungstate with strontium and cerium cations, (Sr,Ce)WO$_4$, was synthesized. As much as 35% Ce could be inserted into the structure, leaving $\frac{1}{7}$ of the (Sr,Ce) cation sites vacant. Partial ordering of Sr and Ce, with atomic displacements, were shown by high-resolution electron microscopy. Two-dimensional incommensurate modulations occur in this material, in small domains 20 nm in size. The band gap of this compound is significantly lower than the band gap of SrWO$_4$ and this was related to the distortions of WO$_4$ and (Sr,Ce)O$_8$ polyhedra. The band gap value of 3.2 eV makes Sr$_{1/2}$Ce$_{5/14}$□$_{1/7}$WO$_4$ a promising candidate for violet luminescence.

1. Introduction

Scheelite molybdates or tungstates are known to be chemically stable luminescent compounds as well as good ionic conductors. In the last decade, their potential use as light emitting materials was explored and many new scheelite compounds were synthesized, by adding lanthanide cations in the structure (Abakumov *et al.*, 2014; Morozov *et al.*, 2013; Nogueira *et al.*, 2013; Jiang *et al.*, 2015). The binary scheelite tetragonal structure of the general formula ABO_4, (space group $I4_1/a$) corresponds to (A^{2+}, B^{6+}) and the cation/anion ratio $[A]/[BO_4]$ is equal to 1. The structure, shown Fig. 1, can be described as a piling up of layers along the c axis built from $[BO_4]$ tetrahedra and $[AO_8]$ polyhedra sharing vertices. This structure easily accommodates cations with different oxidation states for A and B as in BiVO$_4$ (A^{3+}, B^{5+}), ZrGeO$_4$ (A^{4+}, B^{4+}) or AgIO$_4$ (A^+, B^{7+}). When the cation/anion ratio is other than 1, the tetragonal structure of binary tungstate (B = W) or molybdate (B = Mo) scheelite can be distorted into a monoclinic structure as in Ce$_2$W$_3$O$_{12}$ (A^{3+}, B^{6+}) (Arab *et al.*, 2013) or an orthorhombic one as in Ce$_{10}$W$_{22}$O$_{81}$ (Patout *et al.*, 2014). Ternary scheelites refer to compounds with a general formula $(A, A')_n(BO_4)_m$. Most of them are built with a charge difference of 2 between A and A' cations such as (Ag,RE)(MoO$_4$)$_2$ and (Li,RE)(MoO$_4$)$_2$, where RE is a rare earth element (Abakumov *et al.*, 2014). The charge difference is usually accommodated by cation vacancies on A sites, with or without cation ordering or incommensurate modulations (Abakumov *et al.*, 2014; Albino *et al.*, 2012; Culver *et al.*, 2015). Ternary scheelites with a charge difference of 1 are uncommon, and apart from a lead–lanthanide-based compound (Takai *et al.*, 2004), only (Ca,Eu)(BO_4)$_2$ and (Sr,Eu)(BO_4)$_2$ have been extensively studied (Abakumov *et al.*, 2014; Jiang *et al.*, 2015).

Among rare earth compounds with the scheelite structure, rare earth tungstates exhibit excellent thermal and chemical stability. Tungstates have been proven to be good host lattices for the luminescence of lanthanide ions (Zhou *et al.*, 2014). Eu^{3+} is a commonly used luminescent activator and Eu^{3+}-activated $SrWO_4$ is an efficient light emitting diode (Jiang *et al.*, 2015). An interesting alternative to Eu^{3+} is Ce^{3+} because of a potential tunable light emission. The light emission of Ce^{3+} varies from ultraviolet to orange, depending on the crystal field (Zhu *et al.*, 2016; Li *et al.*, 2008). The mechanism of Ce light emission is usually linked to the interaction of the incomplete $4f$ shell energy levels of Ce with the band state of the host lattice (Roy *et al.*, 2010). The determination of the band gap is one way to obtain information on the potential optical properties of a compound. As the band gap value is also linked to the structural defects around the lanthanide ions, which are promoted by the distortions of angles and bond distances within different polyhedra clusters (Cavalcante *et al.*, 2012; Rosa *et al.*, 2008; Lacomba-Perales *et al.*, 2008), structural investigations are needed to understand the band gap values.

The aim of this work was to synthesize an $(Sr,Ce)WO_4$ ternary scheelite compound with different optical properties compared with those of the binary scheelite $SrWO_4$. A complexing method was used to synthesize powders of binary $SrWO_4$, and $(Sr,Ce)WO_4$ ternary tungstate scheelites. Rietveld refinements of the X-ray diffraction patterns were performed to obtain accurate cell parameters and atomic distances. Electron diffraction and high-resolution electron microscopy gave access to the incommensurate modulations and cation ordering. The chemical composition was determined by energy-dispersive spectroscopy (EDS) and the cation valence by electron energy-loss spectroscopy (EELS). UV–visible diffuse reflectance spectroscopy (DRS) was used to determine the energy band gap.

We show that $(Sr,Ce)WO_4$ has an incommensurate modulated structure linked to partial ordering of Sr^{2+} and Ce^{3+}. The

influence of the structure on the band gap values is discussed in terms of bonds distances and angles splitting.

2. Experimental procedures

2.1. Synthesis

The powders were synthesized by the so-called EDTA-citrate complexing method (EDTA is ethylene-diaminetetraacetic acid). This method has already been used to obtain binary tungstates $SrWO_4$ and $Ce_2W_3O_{12}$ (Arab *et al.*, 2013) and was adapted in this work to synthesize ternary tungstates. Strontium nitrate $[Sr(NO_3)_2]$, cerium(III) nitrate hexahydrate $[Ce(NO_3)_3 \cdot 6H_2O]$ and tungsten oxide $[WO_3]$ were used as the cation source. EDTA was diluted in ammonium hydroxide (27% vol.) (NH_4OH) at 313 K with a constant stirring for 15 min. Solutions of 0.3 M strontium and cerium nitrates and WO_3 were added in the solution of the EDTA/NH_4OH in various proportions and stirred for 15 min again. Then 0.45 M citric acid was added to initiate the complexation reaction at a temperature of 353 K and at pH = 9. The reaction time lasted 3 h until the appearance of a gel-like precipitate. This gel was subjected to a heat pretreatment at a temperature of 503 K for 3 h to remove waste liquids and volatiles, leading to the formation of a black powder. The final annealing was performed at 1273 K for 5 h, a temperature ensuring the crystallization of the gel, leading to yellowish white powders.

2.2. Structural and chemical characterization

Transmission electron microscopy (TEM) and high-resolution electron microscopy (HREM) were performed with a conventional Tecnai 200 kV microscope and a Titan FEG 300 kV C_s-corrected microscope equipped with a Gatan imaging filter. Simulated HREM images were calculated using the multislice program *JEMS*. The parameters used for simulations of images taken with the 300 kV microscope were $C_s = -1.9$ μm, $C_c = 2$ mm, $\frac{1}{2}\alpha = 1$ mrad, $\Delta E = 0.7$ eV. The chemical composition of the ternary tungstate was determined using EDS. Binary compounds $SrWO_4$ and $Ce_2W_3O_{12}$ were used as standards for the determination of the $K_{Sr,W}$ and $K_{Ce,W}$ factors. The statistical study of chemical homogeneity of the powder consisted in 20 EDS analyses on randomly chosen individual grains. EELS gave access to the valence of cerium in the ternary compound. Spectra were acquired in the diffraction mode, with a 0.03 eV per channel resolution.

X-ray powder diffraction (XRD) patterns were collected in the classical θ–2θ mode, with an Empyrean Panalytical diffractometer, with a Cu anti-cathode (λ $K_{\alpha 1} = 0.154056$ nm). Rietveld refinements with the software *FullProf* (Rodríguez-Carvajal (1993) were performed, starting from data CIF files found in literature, and cell parameters, atomic positions, as well as site occupations, were extracted. The experimental profiles were fitted with the most suitable pseudo-Voigt analytical function taking into account the line broadening function and the symmetric part of the instrumental function.
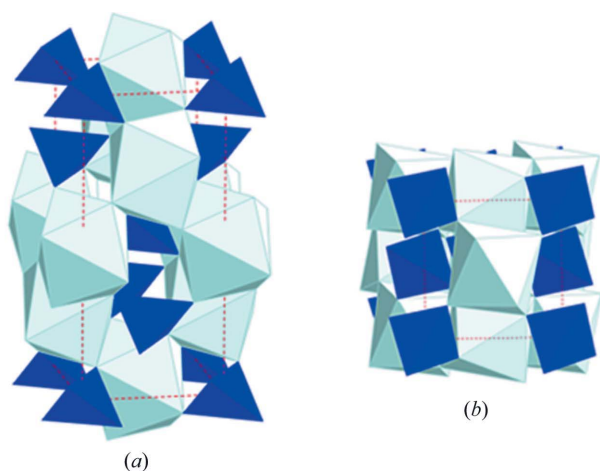

Figure 1
ABO_4 scheelite structure: (*a*) drawing of the unit cell showing the piling up along the *c* axis of edges-linked AO_8 polyhedra and (*b*) drawing of the unit cell along [001] showing that the BO_4 tetrahedra and the AO_8 polyhedra are linked by vertices.

2.3. Optical properties

The band gap values were obtained using the UV–vis diffuse reflectance spectra. The spectra of the different samples were recorded using a Perkin Elmer LAMBDA UV–vis–IR spectrometer along with a 150 mm integrating sphere. A given powder was compacted in a manual press into a 1.2 cm powder cup and then clamped on the external port of the integrating sphere. The measurements were performed in the range of 250–800 nm at room temperature with a resolution of 0.08 nm. The baseline was determined using a calibrated reflectance standard to achieve a reflectance accuracy of 0.5%.

3. Results

3.1. Chemical composition

The mean composition of the ternary compound was found to be $Sr_{0.50}Ce_{0.35}WO_4$, also written as $Sr_{1/2}Ce_{5/14}\square_{1/7}WO_4$, emphasizing the occurrence of cation vacancies. Although the majority of ternary tungstates and molybdates are stoichiometric, ternary scheelite compounds with cation vacancies have already been reported (Abakumov *et al.*, 2014). Ce^{3+} may be partially oxidized into Ce^{4+} and so the valence state of cerium in $Sr_{0.50}Ce_{0.35}WO_4$ was determined by EELS. Ce^{4+} and Ce^{3+} $M_{4,5}$ core-loss edges can unambiguously be distinguished due to differences in shape, intensities and energies (Garvie & Buseck, 1999). The Ce^{4+} $M_{4,5}$-edges consist in two main symmetrical peaks situated at 884 eV and 901.6 eV and two satellites peaks of lower intensities at 889.2 eV and 906.7 eV. In contrast, the Ce^{3+} M_4-edge is asymmetrical with features at 896.6, 898.4 and 899.7 eV and the Ce^{3+} M_5-edge shows a broad maximum from 881.7 to 882.3 eV. Apart from the shape and energy positions of the energy-loss peaks, the branching ratio, defined as the intensity ratio $I(M_5)/[I(M_4) + I(M_5)]$, can be used to distinguish between Ce^{3+} (branching ratio 0.55) and Ce^{4+} (branching ratio 0.49). Fig. 2 shows a characteristic EELS spectrum, acquired on a single grain of the ternary powder. The best fit was obtained with two peaks at 882 and 883 eV for
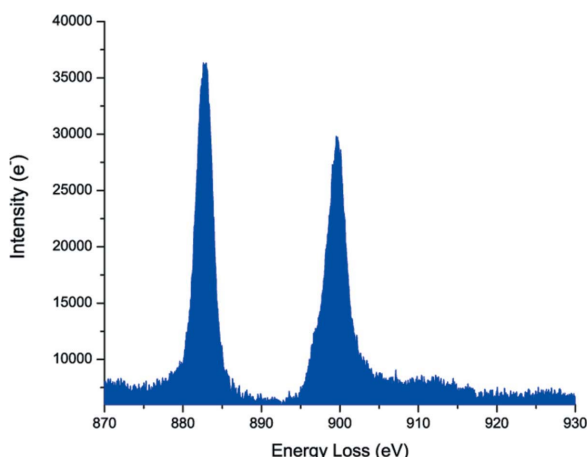
the M_5-edge and three peaks at 896.9, 898.5 and 899.8 eV for the M_4-edge, indicating the cerium is in a 3+ valence state in the ternary scheelite compound. However, the occurrence of two peaks around 883 eV and a branching ratio of 0.53 indicate the presence of Ce^{4+}. Assuming the linear relation between branching ratio and relative amount of Ce^{4+} proposed by Garvie & Buseck (1999), one can estimate the Ce^{4+} amount to be around 30%.

3.2. Electron diffraction

The main spots of the electron diffraction (ED) pattern, taken under different zone axes, could all be indexed in the tetragonal scheelite structure. Fig. 3 presents high-symmetry ED patterns, with [001], [100], [1$\bar{1}$0] and [111] zones axes indexed in the tetragonal structure. In the ED pattern taken along [001] (Fig. 3a), the main spots exhibit the characteristic fourfold symmetry of the tetragonal structure along **c**, but the weaker spots cannot be indexed with integer indices. They correspond to two incommensurate vectors, $\mathbf{q}_1 = 0.54\mathbf{a}^* + 0.82\mathbf{b}^*$, $\mathbf{q}_2 = -0.82\mathbf{a}^* + 0.54\mathbf{b}^*$, thus to a two-dimensional structure modulation, which led to an indexing of the different ED patterns in a $(3 + 2)$-dimensional superspace group with five indices (van Smaalen, 2007). Spots, indexed $(00l00)$ with $l = 2n$, that are forbidden in the space group $I4_1/a$ of the tetragonal scheelite structure, can be observed in Figs. 3(b) and (c). During tilt experiments, these spots do not vanish, excluding a double diffraction phenomenon. A reduction in symmetry must then be considered from $I4_1/a$ to $I\bar{4}$ (No. 82). This symmetry loss has already been observed for ternary scheelite molybdates such as $(Na, Gd)MoO_4$ (Abakumov *et al.*,

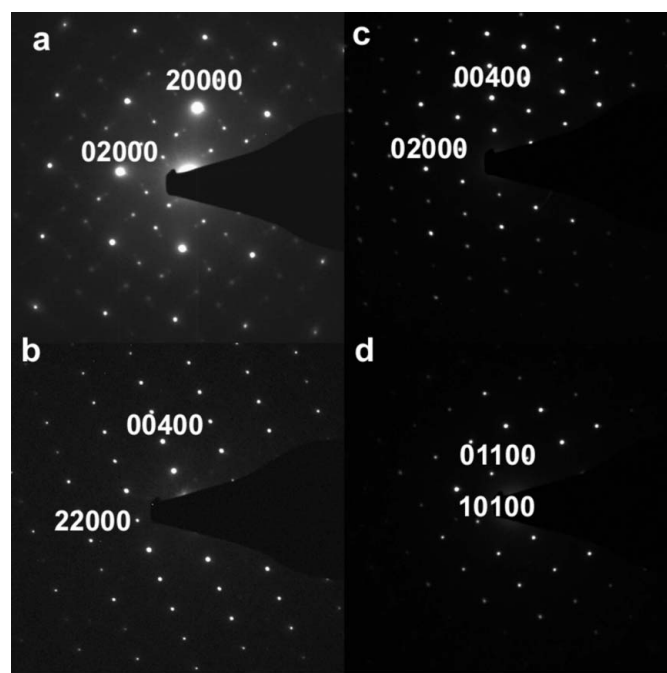**Figure 2**
Cerium $M_{4,5}$ core-loss edge of $Sr_{0.50}Ce_{0.35}WO_4$.

Figure 3
High-symmetry electron diffraction patterns of the incommensurately modulated $Sr_{0.50}Ce_{0.35}WO_4$, along the zone axes [001] (a), [1$\bar{1}$0] (b), [100] (c), [11$\bar{1}$] (d).

2014; Pinheiro & Abakumov, 2015) and (LiYb)MoO$_4$ (Volkov *et al.*, 2005). Thus, the superspace group for Sr$_{0.50}$Ce$_{0.35}$WO$_4$ was identified as $I\bar{4}$ ($\alpha,\beta,0,-\beta\alpha0$)00, with $\alpha = 0.54$ and $\beta = 0.82$. Fig. 4 is part of the [001] pattern, where the two incommensurate vectors $\mathbf{q}_1$ and $\mathbf{q}_2$ are drawn: all the weak spots in the ED pattern can be indexed using $\mathbf{q}_1$ and $\mathbf{q}_2$. Modulated structures are not uncommon in $(A,A')_n(BO_4)_m$ scheelite compounds (B = Mo or W) and an exhaustive overview of them is given by Abakumov *et al.* (2014). This overview was realised in order to study the origin of these modulations, which were linked to the difference in cation sizes, the ordering of the A and A' cations and the presence of cations vacancies in the A sublattice. With a radius difference of $\Delta r = 0.1$ Å between Sr^{2+} and Ce^{3+}, and $\frac{1}{7}$ of vacancies, Sr$_{1/2}$Ce$_{5/14}$□$_{1/7}$WO$_4$ belongs to the same group of partially ordered scheelites as Na$_{2/7}$Gd$_{4/7}$□$_{1/7}$MoO$_4$ (Abakumov *et al.*, 2014). The same modulation vectors $\mathbf{q}_1 = 0.54\mathbf{a}^* + 0.82\mathbf{b}^*$ and $\mathbf{q}_2 = -0.82\mathbf{a}^* + 0.54\mathbf{b}^*$ are observed for these structures, but the charge difference Δq between A and A' cations is $\Delta q = 2$ (Na$^+$, Gd^{3+}) in one case and $\Delta q = 1$ in the other one (Sr^{2+}, Ce^{3+}). Another difference is that two-dimensional incommensurate modulations were observed in molybdates with tetragonal structure but not in tungstate scheelites. In contrast, ternary tungstate scheelites usually adopt a (3 + 1)-dimensional modulated monoclinic structure (Morozov *et al.*, 2013). Thus, one can conclude that two-dimensional modulations are linked to a small Δr and vacancies on A sites, but not to Δq, the charge difference between A and A' cations. Moreover, these modulations can occur in tungstates, not only in molybdates.

3.3. High-resolution electron microscopy

High-resolution electron microscopy (HREM) observations were performed along the [001] direction, where the projected structure corresponds to mixed columns of Sr, Ce and W cations (see Fig. 5a) and along [111], where the projected structure corresponds to distinct atomic columns for the (Sr,Ce) cations and for W (Fig. 5b).

Fig. 6 shows an HREM image taken along [001], as well as a fast Fourier transform (FFT) image and a filtered image. The FFT image is similar to the diffraction pattern in Fig. 4, with the same incommensurate spots. FFT performed on different regions of the HREM image do not always exhibit these spots, which indicate that modulations are localized in domains. The filtered image using the incommensurate spots confirms a 10–20 nm domain-type structure. The filtered image, using Bragg spots 20000 and 02000, has an enhanced contrast compared with the original image, shows no defects and can be interpreted in terms of atomic columns of cations.

In order to study a possible ordering of Sr and Ce, HREM images were taken along [111], using a 300 kV microscope with C_s correction. This projection direction allows us to interpret HREM images in terms of atomic columns of W, Sr, Ce (Fig. 5b). In particular, along the trace of (112) planes, there will be successively two W columns and two (Sr,Ce) columns. Fig. 7 shows an HREM image taken along [111] where thickness variations give rise to different motifs. The
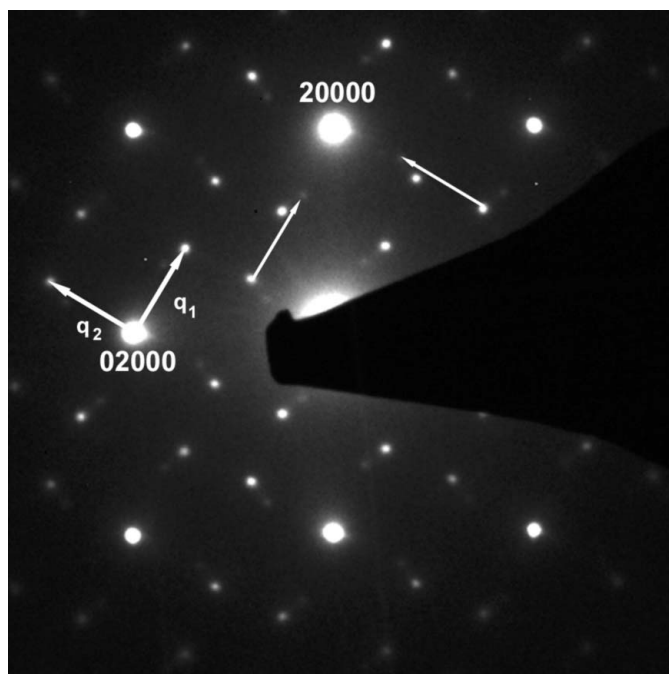

Figure 4
Part of [001] electron diffraction pattern, showing that all supplementary spots are due to the incommensurate vectors $\mathbf{q}_1$ and $\mathbf{q}_2$.
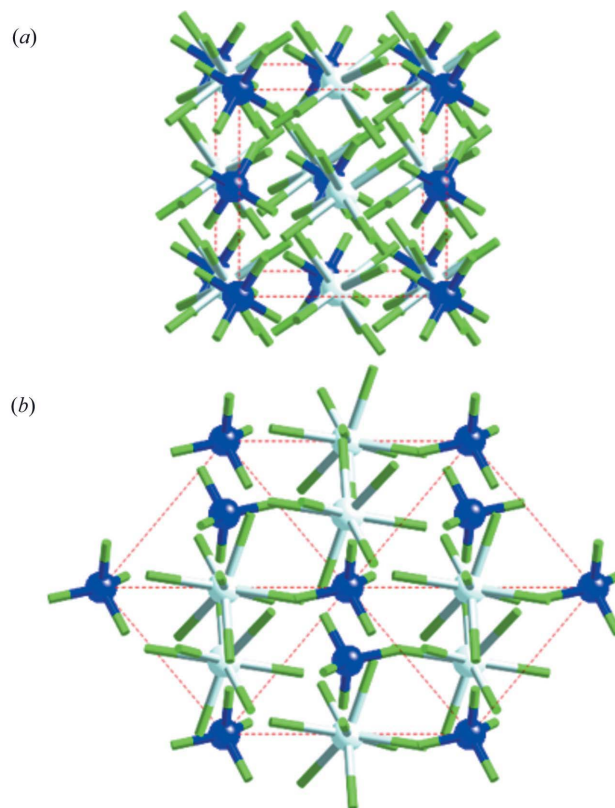

Figure 5
Projection of the ABO_4 structure along two different crystallographic (a) [001] and (b) [111]. A cations are drawn as light blue and B cations are dark blue, and the $A-$O and $B-$O links are drawn as sticks.
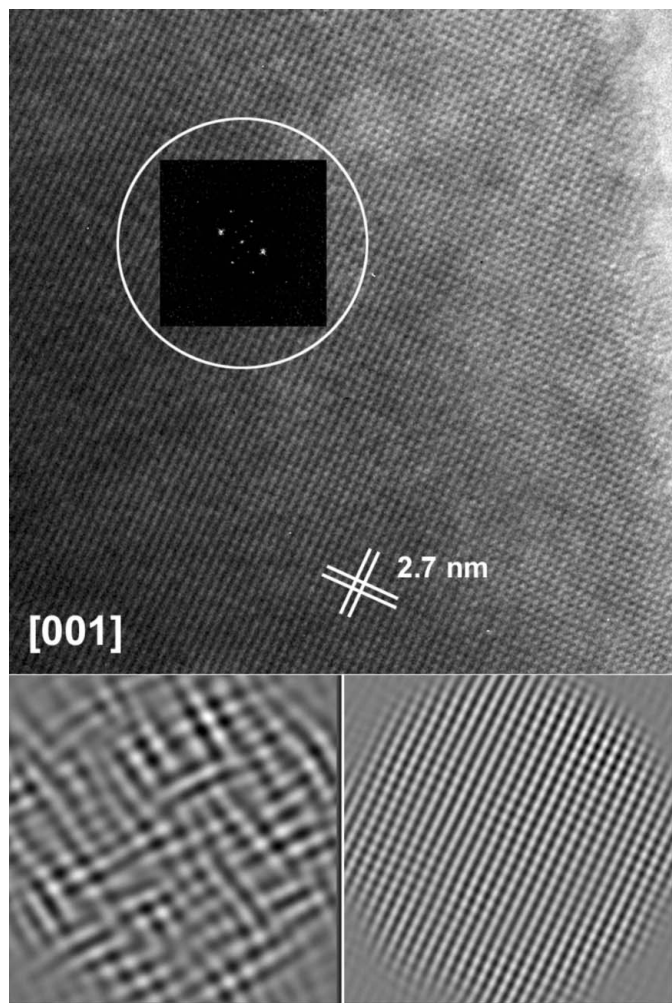
Figure 6
HREM image taken along [001], with FFT and filtered images shown below.
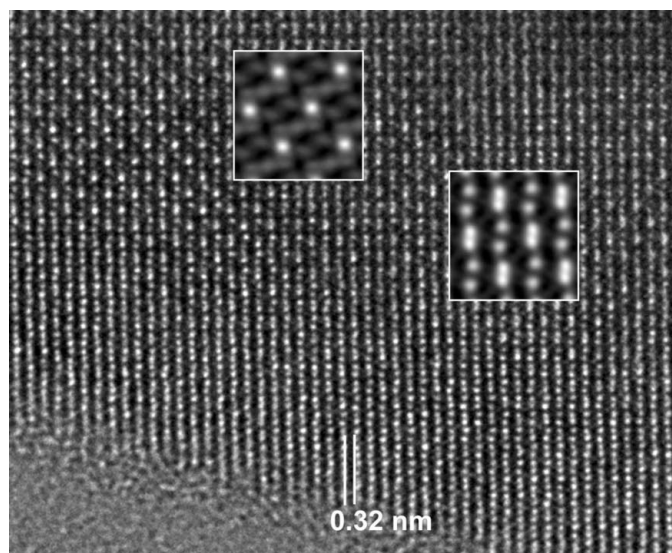

Figure 7
HREM image taken along [111]. The inset show two characteristic patterns.

Table 1
Atom coordinates of Sr, Ce, W and O in $I4_1/a$ and $I\bar{4}$ space groups.

Space group	Atom	Site	Coordinates
$I4_1/a$	Sr, Ce	4b	$0, 0, \frac{1}{2}$, $0, \frac{1}{2}, \frac{3}{4}$
	W	4a	$0, 0, 0$, $0, \frac{1}{2}, \frac{1}{4}$
	O	16f	x, y, z
$I\bar{4}$	Sr, Ce	2b	$0, 0, \frac{1}{2}$
	Sr, Ce	2c	$0, \frac{1}{2}, \frac{1}{4}$
	W	2a	$0, 0, 0$
	W	2d	$0, \frac{1}{2}, \frac{3}{4}$
	O_1, O_2	8g	x, y, z

two insets correspond to filtered images from a thin part and a thick part of the sample. In the thin part of the sample, the position of the bright spots as well as their intensity clearly varies along the trace of the (112) planes, suggesting different atomic occupation. Simulated HREM images were calculated using two structural models and compared with the filtered images. Both structural models were based on the $I\bar{4}$ space group deduced from the ED study. The first model (model 1) corresponds to a disordered scheelite structure; Sr and Ce cations occupy randomly the same 2b and 2c sites, and W is on the 2a and 2d sites. Morozov *et al.* (2012) have already used this structural model for $Na_{2/7}Gd_{4/7}MoO_4$. In the second model (model 2), the Sr cations occupy the 2b site whereas the Ce cations are on 2c sites. The chemical composition was taken into account; thus vacancies were statistically distributed on 2b and 2c sites for both models. The atomic positions are summarized in Table 1.

The pattern observed in the thick part of the sample can be solely simulated with the structural model where Ce and Sr are ordered, for a thickness of 5–7 nm (Fig. 8). The pattern observed in the thin part can, at first sight, be simulated for both disordered and ordered models, but the intensity variation observed along one row corresponds strictly to different site occupation for strontium and cerium, as can be seen in Fig. 8, where the projected structure is superimposed to a simulated one for a weak thickness of 3 nm. Thus, HREM has proved experimentally the ordering of strontium and cerium atoms in $Sr_{0.50}Ce_{0.35}WO_4$.
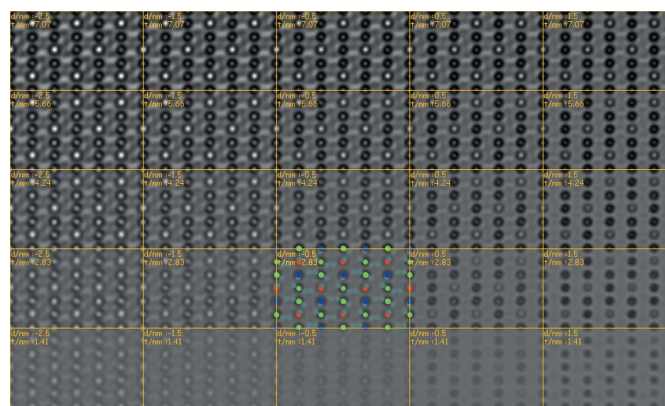

Figure 8
Map of images simulated (model 2). The defocus d varies from 2.5 nm to −1.5 nm, the thickness t from 1.4 nm to 7 nm. Projected atoms are represented as dots, Sr = blue, Ce = red, W = green

3.4. Crystal structure refinements (X-ray diffraction)

Fig. 9 shows the XRD patterns of the binary $SrWO_4$ (Fig. 9a) and of the new ternary $Sr_{0.50}Ce_{0.35}WO_4$ (Fig. 9b) compounds. The diagrams correspond to well crystallized single phases without residual compounds. The phase identification showed that both tungstates exhibit XRD diagrams characteristic of the tetragonal scheelite structure. In particular, the splitting of the high-angle peaks induced by a monoclinic structure was not observed.

We performed different Rietveld refinements of the XRD patterns, according to electron microscopy results. The binary compound $SrWO_4$ was refined in the $I4_1/a$ space group. The ternary compound $Sr_{0.50}Ce_{0.35}WO_4$ was refined in the $I4_1/a$ space group and in the $I\bar{4}$ space group, with a random occupation of A sites by Ce^{3+} and Sr^{2+} (the so-called disordered scheelite). The occupation rate of the A sites was fixed to 50% for Sr and 35% for Ce, in accordance with EDS results. In both space groups, the cations occupy fixed Wyckoff positions (see Table 1) and only the coordinates of oxygen atoms were refined. The refinements were initiated using CIF files already published (Pereira *et al.*, 2015; Abakumov *et al.*, 2014). The refined cell parameters, oxygen coordinates and reliability factors are reported in Table 2.

The refinements in the $I4_1/a$ space group provide a good agreement with the experimental data for the binary and the ternary compounds, with acceptable reliability factors. The cell parameters of the ternary scheelite $Sr_{0.50}Ce_{0.35}WO_4$ are
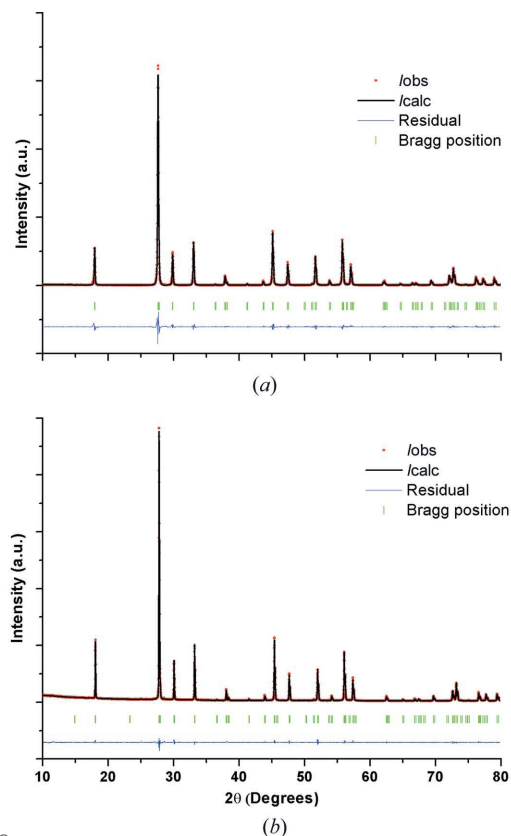
Table 2
Refinement results for the binary $SrWO_4$ and the ternary $Sr_{0.50}Ce_{0.35}WO_4$ compounds using two different space groups.

Compound	$SrWO_4$	$Sr_{0.50}Ce_{0.35}WO_4$	$Sr_{0.50}Ce_{0.35}WO_4$	
Space group	$I4_1/a$	$I4_1/a$	$I\bar{4}$	
Cell parameters (Å)	$a = 5.416\,(8)$,	$a = 5.394\,(2)$,	$a = 5.394\,(2)$,	
	$c = 11.975\,(0)$	$c = 11.884\,(7)$	$c = 11.884\,(7)$	
Cell volume (Å^3)	351.363	345.809	345.814	
Oxygen coordinates	O (16f)	O (16f)	O_1 (8g)	O_2 (8g)
x	0.2504	0.3559	0.2533	0.6492
y	0.1106	0.0135	0.1395	0.7892
z	0.04121	0.2919	0.9250	0.1601
Reliability factors				
R_p	9.48	6.22	6.68	
R_{wp}	13.4	7.32	7.53	
R_{exp}	7.88	5.07	5.26	
χ^2	2.91	2.08	2.05	
R_{Bragg}	3.59	3.12	2.76	

smaller than those of the binary $SrWO_4$, with a shrinkage of the unit cell of about 1.4% in volume. This is in agreement with the substitution of Sr^{2+} by Ce^{3+}, which has a smaller radius ($\Delta r = -0.1$ Å) and the induced cation vacancies. The loss of symmetry from space group $I4_1/a$ to $I\bar{4}$, corresponds to a splitting of each atomic position (see Table 1). Thus, the cations were distributed on the different sites according to model 1 (no ordering of Sr and Ce). Again, the reliability factors show a good agreement between the calculated and the experimental diffraction patterns. The differences in the reliability factors for the two refinements of the $Sr_{0.50}Ce_{0.35}WO_4$ structure are too small to discriminate between the two possible space groups (Nos. 82 and 88). This can be related to the polycrystalline character of our samples with heterogeneous size distribution in the nanometre range. Thus, investigations of a possible cation ordering through Rietveld refinements of XRD diagrams were meaningless.

The variation in the atomic coordinates observed for oxygen atoms, gives rise to different distortions of the polyhedra as can be seen in Table 3, which summarizes the $A-O$ and $W-O$ bond lengths and angles. The cerium insertion in the $SrWO_4$ scheelite structure leads to a contraction of WO_4 tetrahedra and an expansion of AO_8 polyhedra.
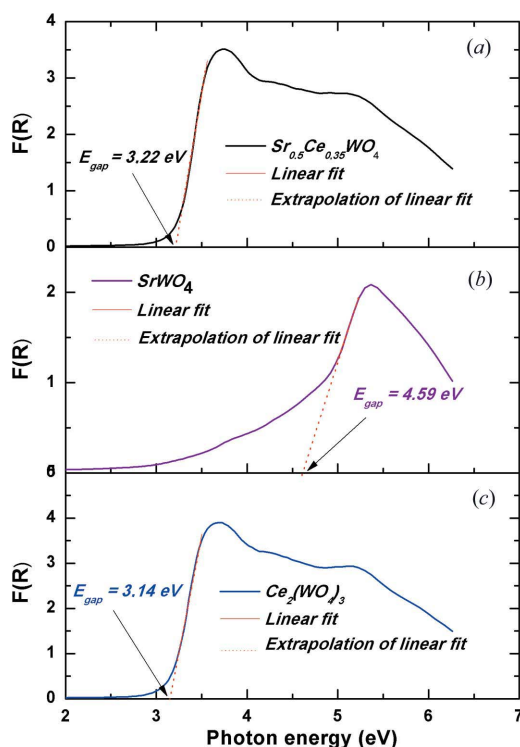
Basically, the $SrWO_4$ binary compound presents a main $W-O$ distance of 1.8408 Å and two characteristic $O-W-O$ angles values of 107° and 114°. The $W-O$ distance decreases to 1.7903 Å in the $Sr_{0.50}Ce_{0.35}WO_4$ structure in the $I4_1/a$ space group but the $O-W-O$ angles remain the same, 107.7° and 113°. The $A-O$ bond length increases, showing the WO_4 contraction is accompanied by an AO_8 expansion, and the $O-A-O$ angles do not change significantly. In contrast, the refined structure with the $I\bar{4}$ space group shows much more WO_4 and AO_8 distortion. In this space group there are two $W-O$ distances of 1.7964 and 1.7554 Å. The $O-W-O$ angles deviate much more from the ideal tetrahedral angle of 109.9°, with values of 104, 105, 111 and 120°, respectively. Similarly, the AO_8 polyhedron has four different $A-O$ bond lengths and different $O-A-O$ angles, as reported in Table 3. Thus, the structure refined in space group $I\bar{4}$ is much more distorted than the corresponding one in $I4_1/a$.

Figure 9
XRD patterns of (a) $SrWO_4$ and (b) $Sr_{0.5}Ce_{0.35}WO_4$: observed and refined profiles.

Table 3
Bond lengths and angles in [WO₄] and [AO₈] octahedra.

Compound		SrWO₄	Sr₀.₅₀Ce₀.₃₅WO₄	Sr₀.₅₀Ce₀.₃₅WO₄	
Space group		$I4_1/a$	$I4_1/a$	$I\bar{4}$	
Polyhedra	WO₄				
Bond (Å)	W—O	1.840 (8)	1.790 (4)	1.755 (4)	1.796 (4)
Angle (°)	O—W—O	106.9	107.7	105.0	104.2
		114.6	113.1	111.7	120.5
Polyhedra	AO₈				
Bond (Å)	A—O1	2.533 (4)	2.561 (4)	2.519 (5)	2.581 (2)
	A—O2	2.571 (6)	2.585 (0)	2.588 (9)	2.675 (1)
Angle (°)	O—A—O	68.8	67.9	68.3	65.4
		74.8	73.5	70.2	72.6
		75.6	77.5	79.5	76.8
		76.1	78.5	85.38	77.7
		98.6	98.4	97.2	99.2
		128.3	126.8	122.7	130.5
		134.5	135.1	138.5	132.9
		150.5	151.0	152.8	148.9

3.5. Optical properties

For potential optical applications (luminescence and photocatalysis), the band gap energies of the ternary scheelite structure, as well as those of the two binary compounds $SrWO_4$ and $Ce_2(WO_4)_3$, were measured using UV–vis DRS at room temperature. This allowed us to discuss the contribution of the insertion of cerium in the scheelite structure. Fig. 10 shows the UV–vis spectra of $Sr_{0.50}Ce_{0.35}WO_4$, $SrWO_4$ and $Ce_2(WO_4)_3$. Large bands were observed for all spectra after 3 eV. According to theoretical calculations reported in the literature, tungstate scheelite materials such as $SrWO_4$ exhibit an optical absorption band due to direct electronic transition (Zhang *et al.*, 1998), which occurs through excitation of electrons from the valence band to the conduction band (Hwang *et al.*, 2003). UV–vis spectra show that the absorption band obtained for $Ce_2(WO_4)_3$ is more intense than that of $Sr_{0.50}Ce_{0.35}WO_4$ and $SrWO_4$. The intense band observed in the visible region is attributed to the electronic transition of the cerium cation present in the sample.

The energy band gap is obtained by using the Kubelka–Munk method which consists in plotting $F(R_\infty)$ *versus* photon energy. The band gap is deduced by extrapolating the $F(R_\infty)$ profile using a linear fitting method. R_∞ designates the reflectance of the sample at infinite thickness and $F(R_\infty)$ the absolute diffuse reflectance of the sample, which corresponds to the conversion of the reflectance measurements R_∞ according to the following equation

$$F(R_\infty) = \frac{(1-R_\infty)^2}{2R_\infty} = \frac{K}{S},$$

where K is the molar absorption coefficient and S is the scattering coefficient.

The absorption band gap values for $Sr_{0.50}Ce_{0.35}WO_4$, $SrWO_4$ and $Ce_2(WO_4)_3$ were found to be 3.22, 4.59 and 3.14 eV respectively. The energy gap of the $SrWO_4$ is in accordance with the theoretical result of 4.51 eV (Song *et al.*, 2009). In the case of $Ce_2(WO_4)_3$, the band gap energy of 3.14 eV is in agreement with the one obtained using DFT calculations in a complex system based on a polyoxometalate $[Ce(W_5O_{18})_2]^{8-}$ cluster with CeO_8 polyhedra (Roy *et al.*, 2010). The calculated molecular orbital diagram shows that the electron density consists on the O2*p* atomic orbital for the HOMO and the Ce 4*f* orbitals for the LUMO, with a band gap of 3.28 eV. Variations of the gap values can be linked to different factors such as shape and crystallite size (Alivisatos, 1996), lattice parameters (Yang *et al.*, 2015) and degree of structural disorder in the lattice (Rosa *et al.*, 2008; Lacomba-Perales *et al.*, 2008). For $SrWO_4$, the band gap value shows that the maximum of the valence band can be mainly attributed to O2*p* levels, whereas the bottom of the conduction band is mainly composed of W 5*d* levels. The Sr 5*s* levels are mainly distributed in the conduction band and, thus, do not contribute to the band gap (Song *et al.*, 2009; Arora & Chudasama, 2006). The insertion of cerium in the host structure of $SrWO_4$ can promote different energy distribution at intermediate levels, linked to the 4*f*, 5*d* and 6*s* atomic orbitals, in the band gap near the valence and conduction bands. Combining all these elements, the band structure of $Ce_{0.35}Sr_{0.50}WO_4$, would consist in a valence band with mainly O2*p* states and the bottom of the conduction band mainly composed of Ce 4*f* levels.

To further understand the optical properties evolution of the scheelite structures, the band gap is discussed in terms of microstructural parameters such as bond distance and angles of the polyhedra and the crystallite size.

Generally, it is admitted that the band gap of semiconductors increases when the particle size decreases (Lacomba-Perales *et al.*, 2008). According to a statistical study of grain size distribution based on microscopy images (not

Figure 10
UV–vis spectra of $Sr_{0.5}Ce_{0.35}WO_4$, $SrWO_4$ and $Ce_2(WO_4)_3$ powders.

reported here), the mean grain size is the same for the different powders and the low band gap value of the ternary compound cannot be attributed to a size effect. Concerning the influence of cell parameters on the band gap value, the contraction of 1.4% in volume of the cell from $SrWO_4$ to $Sr_{1/2}Ce_{5/14}\square_{1/7}WO_4$ should induce a small decrease of the band gap (Lacomba-Perales *et al.*, 2008).

According to the data in Table 3, the band gap decreases with decreasing W—O bond lengths and increasing of A(Sr,Ce)—O bonds lengths. In the same way, all O—W—O and O—A—O angles are much more distorted in the ternary compound refined in the $I\overline{4}$ space group. These changes in bonds and angles correspond to the W—O and A(Sr, Ce)—O stretching and twisting motions. They can be described as a combination of the symmetric and antisymmetric stretches of the oxygen atom bonds in the polyhedra WO_4 and AO_8. In addition to the vacancies, the presence of cerium ions Ce^{4+} in the structure should induce even more distortions, favouring the appearance of intermediate levels in the band gap. As a consequence, the $Ce_{0.35}Sr_{0.50}WO_4$ scheelite structure gap energy decreases from 4.59 to 3.22 eV, a value very close to the band gap value of $Ce_2(WO_4)_3$.

4. Conclusion

In the present work, a ternary (Sr,Ce)WO_4 compound has been synthesized using a modified EDTA–citrate method. The structure was identified as a tetragonal scheelite and the XRD patterns showed well crystallized single phases up to 35% at. of cerium. Electron diffraction and high-resolution electron microscopy techniques showed the incommensurate modulations linked to partial ordering of Sr^{2+} and Ce^{3+}, and the loss of symmetry from the $I4_1/a$ space group to the $I\overline{4}$ one. The Rietveld refinement results with the $I\overline{4}$ space group revealed distortions of the AO_8 polyhedra, *i.e.* the local environment of Ce^{3+}. The band gap of the ternary compound is significantly lower than the band gap of $SrWO_4$ and this was related to the $4f$ atomic orbitals of Ce and the induced crystallographic distortions linked to the incommensurate modulations. The band gap value of 3.2 eV makes $Sr_{1/2}Ce_{5/14}\square_{1/7}WO_4$ a promising candidate for violet luminescence.

Acknowledgements

References

Abakumov, A. M., Morozov, V. A., Tsirlin, A. A., Verbeeck, J. & Hadermann, J. (2014). *Inorg. Chem.* **53**, 9407–9415.

Albino, M., Pechev, S., Veber, P., Velazquez, M. & Josse, M. (2012). *Acta Cryst.* C**68**, i7–i8.

Alivisatos, A. P. (1996). *Science*, **271**, 933–937.

Arab, M., Lopes-Moriyama, A. L., dos Santos, T. R., de Souza, C. P., Gavarri, J. R. & Leroux, Ch. (2013). *Catal. Today*, **208**, 35–41.

Arora, S. K. & Chudasama, B. (2006). *Cryst. Res. Technol.* **41**, 1089–1095.

Cavalcante, L. S., Almeida, M. A. P., Avansi, W. Jr, Tranquilin, R. L., Longo, E., Batista, N. C., Mastelaro, V. R. & Li, M. S. (2012). *Inorg. Chem.* **51**, 10675–10687.

Culver, S. P., Greaney, M. J., Tinoco, A. & Brutchey, R. L. (2015). *Dalton Trans.* **44**, 15042–15048.

Garvie, L. A. J. & Buseck, P. R. (1999). *J. Phys. Chem. Solids*, **60**, 1943–1947.

Hwang, D. W., Jae Sung, L., Wei, L. & Se Hyuk, O. (2003). *J. Phys. Chem. B*, **107**, 4963–4970.

Jiang, P., Gao, W., Cong, R. & Yang, T. (2015). *Dalton Trans.* **44**, 6175–6183.

Lacomba-Perales, R., Ruiz-Fuertes, J., Errandonea, D., Martínez-García, D. & Segura, A. (2008). *Europhys. Lett.* **83**, 37002.

Li, Y. Q., Hirosaki, N., Xie, R. J., Takeda, T. & Mitomo, M. (2008). *Chem. Mater.* **20**, 6704–6714.

Morozov, V., Arakcheeva, A., Redkin, B., Sinitsyn, V., Khasanov, S., Kudrenko, E., Raskina, M., Lebedev, O. & Van Tendeloo, G. (2012). *Inorg. Chem.* **51**, 5313–5324.

Morozov, V., Bertha, A., Meert, K. W., Van Rompaey, S., Batuk, D., Martinez, G. T., Van Aert, S., Smet, P. F., Raskina, M. V., Poelman, D., Abakumov, A. M. & Hadermann, J. (2013). *Chem. Mater.* **25**, 4387–4395.

Nogueira, I. C., Cavalcante, L. S., Pereira, P. F. S., de Jesus, M. M., Rivas Mercury, J. M., Batista, N. C., Li, M. S. & Longo, E. (2013). *J. Appl. Cryst.* **46**, 1434–1446.

Patout, L., Jacob, D., Arab, M., Pereira de Souza, C. & Leroux, C. (2014). *Acta Cryst.* B**70**, 268–274.

Pereira, P. F. S., Nogueira, I. C., Longo, E., Nassar, E. J., Rosa, I. L. V. & Cavalcante, L. S. (2015). *J. Rare Earths*, **33**, 113–128.

Pinheiro, C. B. & Abakumov, A. M. (2015). *IUCrJ*, **2**, 137–154.

Rodríguez-Carvajal, J. (1993). *Physica B*, **192**, 55–69.

Rosa, I. L., Marques, A. P. A., Tanaka, M. T., Melo, D. M., Leite, E. R., Longo, E. & Varela, J. A. (2008). *J. Fluoresc.* **18**, 239–245.

Roy, L. E., Ortiz-Acosta, D., Batista, E. R., Scot, E. R., Blair, M. W., May, I., Del Sesto, R. E. & Martin, R. L. (2010). *Chem. Commun.* **46**, 1848–1850.

Song, M., Zhang, Q., Liu, T., Yin, J., Guo, X., Zhang, H. & Wang, X. (2009). *Curr. Appl. Phys.* **9**, 812–815.

Takai, S., Nakanishi, T., Oikawa, K., Torii, S., Hoshikawa, A., Kamiyama, T. & Esaka, T. (2004). *Solid State Ionics*, **170**, 297–304.

van Smaalen S. (2007). *Incommensurate Crystallography*, IUCr Monographs 21. Oxford Science Publications.

Volkov, V., Cascales, C., Kling, A. & Zaldo, C. (2005). *Chem. Mater.* **17**, 291–300.

Yang, X., Fu, Z., Liu, G., Zhang, C. Y., Wei, Y., Wu, Z. & Sheng, T. (2015). *RSC Adv.* **5**, 70220–70228.

Zhang, Y., Holzwarth, N. & Williams, R. T. (1998). *Phys. Rev. B*, **57**, 12738–12750.

Zhou, Y., He, X. H. & Yan, B. (2014). *Opt. Mater.* **36**, 602–607.

Zhu, Q.-Q., Wang, L., Hirosaki, N., Hao, L. Y., Xu, X. & Xie, R.-J. (2016). *Chem. Mater.* **28**, 4829–4839.